


Moisture-Induced Non-Equilibrium Phase Segregation in Triple Cation Mixed Halide Perovskite Monitored by *In Situ* Characterization Techniques and Solid-State NMR

Mohammad Ali Akhavan Kazemi, Nicolas Folastre, Parth Raval, Michel Sliwa, Jean Marie Vianney Nsanzimana, Sema Golonu, Arnaud Demortiere, Jean Rousset, Olivier Lafon, Laurent Delevoye, G. N. Manjunatha Reddy, and Frédéric Sauvage* 

Environmental stability is a major bottleneck of perovskite solar cells. Only a handful of studies are investigating the effect of moisture on the structural degradation of the absorber. They mostly rely on ex situ experiments and on completely degraded samples, which restrict the assessment on initial and final stage. By combining in situ X-ray diffraction under controlled 85% relative humidity, and live observations of the water-induced degradation using liquid-cell transmission electron microscopy, we reveal two competitive degradation paths leading on one hand to the decomposition of state-of-the-art mixed cation/anion ($\text{Cs}_{0.05}(\text{MA}_{0.17}\text{FA}_{0.83})_{0.95}\text{Pb}(\text{Br}_{0.17}\text{I}_{0.83})_3$ (CsMAFA) into PbI_2 through a dissolution/recrystallization mechanism and, on the other hand, to a non-equilibrium phase segregation leading to CsPb_2Br_5 and a Cesium-poor/iodide-rich $\text{Cs}_{0.05-x}(\text{MA}_{0.17}\text{FA}_{0.83})_{0.95}\text{Pb}(\text{Br}_{0.17-2y}\text{I}_{0.83+2y})_3$ perovskite. This degradation mechanism is corroborated at atomic-scale resolution through solid-state ^1H and ^{133}Cs NMR analysis. Exposure to moisture leads to a film containing important heterogeneities in terms of morphology, photoluminescence intensities, and lifetimes. Our results provide new insights and consensus that complex perovskite compositions, though very performant as champion devices, are comparatively metastable, a trait that limits the chances to achieve long-term stability.

1. Introduction

In the last few years, perovskite solar cells (PSCs) became one of the most advanced technology in photovoltaics (PVs), reaching 25.5% certified power conversion efficiency (PCE) in single-junction cells.^[1] This high-performance level, exceeding 80% of the thermodynamic bandgap limit of the perovskite, stems from the maximization of the solar spectrum absorption capability and reduction of the open-circuit voltage deficit through well-adjusted interfacial band level alignment and bulk/interface defects passivation to abate nonradiative recombination processes.^[2] The reduction of interfacial energy losses due to energy misalignment is facilitated given the large richness of cationic and anionic substitution possibilities starting from the prototypical $\text{CH}_3\text{NH}_3\text{PbI}_3$ (MAPbI₃) composition, affording a very precise control of the optoelectronic characteristics. Through a wide exploration of composition, triple cation/double halide formulation $\text{Cs}_{0.05}(\text{MA}_{0.17}\text{FA}_{0.83})_{0.95}\text{Pb}(\text{Br}_{0.17}\text{I}_{0.83})_3$ (CsMAFA) rapidly emerged as one of the most efficient compositions

for single-junction PSC^[3,4] and also as a top cell in a monolithic perovskite/silicon tandem architecture reaching above 29% certified PCE with a slightly bromide richer composition.^[5]

However, the performance enhancement has progressed more rapidly than improving the stability, inhibiting the technology transfer to larger scale. Many efforts are now turned toward this objective through device encapsulation,^[6,7] hydrophobic interfacial layers,^[8] nanoscale 2D/3D structuration,^[9] and defects passivation.^[10–13] Top-down approaches that give further insights into the degradation pathways of the perovskite absorber and device stacks under operational conditions are highly desirable to propose rational ways to improve the stability at different scales from bulk and surface of the materials, interfaces, and finally on the entire device. Given the complexity in deciphering all possible contributions involved during the degradation, the first step ex situ investigations provide already relevant trends about material weaknesses. For instance, exposure of the conventional MAPbI₃ composition to a humid atmosphere showed rapid decomposition into PbI_2 and gas releases.^[14] Depending on the relative humidity (RH)

M. A. A. Kazemi, N. Folastre, Dr. J. M. V. Nsanzimana, Dr. S. Golonu, Dr. A. Demortiere, Dr. F. Sauvage

Laboratoire de Réactivité et Chimie des Solides (LRCS), UMR CNRS 7314 – Institut de Chimie de Picardie FR 3085, Université de Picardie Jules Verne, 33 rue Saint Leu, Amiens Cedex FR-80039, France

E-mail: frederic.sauvage@u-picardie.fr


P. Raval, Dr. O. Lafon, Dr. L. Delevoye, Dr. G. N. M. Reddy

CNRS, Centrale Lille, UMR 8181, UCCS, Unité de Catalyse et Chimie du Solide, Université de Lille, Université d'Artois, Lille F-59000, France

Dr. M. Sliwa

UMR 8516 – LASIRE – Laboratoire de Spectroscopie pour les Interactions, la Réactivité et l'Environnement, CNRS, Université de Lille, Lille F-59000, France
Dr. J. Rousset

EDF R&D, EDF Lab, Boulevard Gaspard Monge, Palaiseau 91120, France

 The ORCID identification number(s) for the author(s) of this article can be found under <https://doi.org/10.1002/eam2.12335>.

DOI: 10.1002/eam2.12335

level, a phase transition from MAPbI₃ to its lower dimensional 1D MAPbI₃·H₂O (quasi-reversible transition) and then to MAPbI₃·2H₂O has also been reported.^[15–18] This phase transition stems from a strong hydrogen bond formation involving the structural water molecules and the organic network of the perovskite.^[19] The 1D confinement of the carriers in these types of hydrated phases leads to a bandgap widening to 3.1 eV^[17] and significantly shorter excited states lifetimes, which is detrimental for the device performances.^[20] The introduction of inorganic cations such as cesium and the more stable formamidinium in the A site to form mixed cations/anions composition raised new issues related to apparent metastability leading in fine to phase segregation driven by the long-range mobility of the halides in the structure either under illumination^[21–26] or humidity.^[27–29]

Capturing the degradation pathways of perovskites at the molecular-level details provide the highest level of comprehensiveness regarding the material response to a specific external stress. It is fundamentally the most insightful approach to close the gap in degradation understanding, therefore to provide new directions to hamper degradation. In order to achieve this, it calls for advanced in situ characterization techniques to assess a live visualization of the degradation paths. Very recently, in situ X-ray diffraction study under 85% RH and liquid-cell in situ transmission electron microscopy revealed the dissolution/recrystallization process in MAPbI₃ and the key role exerted by the surface defects in the reactivity of water molecules.^[30]

In this work, we reveal and clarify the different steps leading to the phase segregation in Cs_{0.05}(MA_{0.17}FA_{0.83})_{0.95}Pb(Br_{0.17}I_{0.83})₃ composition induced by moisture exposure on the basis of advanced in situ X-ray diffraction, liquid-cell transmission electron microscopy techniques combined with atomic-scale resolved solid-state NMR study.

2. Results

The optical bandgap of Cs_{0.05}(MA_{0.17}FA_{0.83})_{0.95}Pb(Br_{0.17}I_{0.83})₃ (CsMAFA) prepared by spin coating and deposited on glass is 1.63 eV (Figure 1a inset), which is in good agreement with the literature.^[31] The Urbach energy is 87 meV, a value larger than what is typically found for the simplest MAPbI₃ composition. Subjecting the same film to 1000 min under 85% RH without encapsulation leads to a twofold decrease in absorbance below ca. 520 nm. Three main optical transitions are composing the absorption fingerprint of CsMAFA, one sharp transition at ca. 750 nm, a broad transition at ca. 530 nm, and a sharp transition at 420 nm, which are attributed to direct band-to-band transitions at different wave-vector locations in the Brillouin zone of the perovskite.^[29] Three transitions are still observed after aging, however, with very subtle differences, in particular at around 520 nm for which the optical transition turned from a broad to a very sharp transition, suggesting a modification in the origin of this transition, which is at 2.29 eV (Figure S1). As further evidenced in the following, we reasoned that this very sharp transition stems from the direct bandgap of PbI₂, which is substantially formed after exposure to moisture.^[32] The deeper transition in blue becomes significantly weaker in absorbance and is ca. 10 nm red-shifted after aging. This suggests noticeable modifications of the nature of this band-to-band transition and the involved density of states in the dispersion curves. The Tauc plot also shows a slight narrowing in the bandgap value from 1.63 to 1.61 eV without substantial modification of the Urbach energy. Steady-state photoluminescence (PL) shows a maximum red-shift from 778 to 787 nm, which corroborates very well with the optical bandgap narrowing. A

more intense PL after aging is also systematically noticed, as observed previously for MAPbI₃ (Figure 1b).^[30,33,34] Although counter-intuitive at first sight, the greater PL after aging can be accounted to a passivation mechanism of the surface defects by water molecules reducing non-radiative recombination processes.^[35]

In order to grasp relevant insights about the structural evolution of the film upon aging, we carried out in situ X-ray diffraction experiments under 85% RH until 1000 min exposure (Figure 2). At the early stage of aging, that is, before 20 min, only the diffraction peaks belonging to CsMAFA are observed. The peaks at $2\theta = 14.05^\circ, 19.99^\circ, 24.46^\circ, 28.42^\circ, 31.76^\circ,$ and 34.93° correspond to the (110), (200), (202), (220), (310), and (312) planes, respectively. CsMAFA crystallizes into a tetragonal unit cell within *I4/mmm* space group. The refined lattice cell parameters are $a = 8.89(1) \text{ \AA}$ and $c = 12.57(1) \text{ \AA}$, leading to a cell volume of $994.3(1) \text{ \AA}^3$. After 20 min of moisture exposure, the onset of new diffraction peaks at $2\theta = 11.13^\circ, 12.63^\circ, 22.38^\circ, 25.50^\circ, 33.86^\circ,$ and 38.62° is observed, which cannot be ascribed to the Bragg reflections of the *I4/mmm* space group of CsMAFA. The diffraction peaks at $2\theta = 12.63^\circ, 2\theta = 25.50^\circ,$ and 38.62° are ascribed to the (001), (002), and (003) planes of the hexagonal PbI₂ phase. The origin of PbI₂ formation stems from the water-induced decomposition of CsMAFA driven by the higher thermodynamic stability of PbI₂ compared to the bromide counterpart. The nucleation and growth of PbI₂ in the CsMAFA film is highly anisotropic, as indicated by the strong preferential orientation along (001) plane.

After ca. 1 h of aging, another degradation phase is emerged with a set of diffraction peaks at $2\theta = 11.13^\circ, 22.38^\circ,$ and 33.86° corresponding to the same family of planes. This new phase is attributable to the layered CsPb₂Br₅ structure, which crystallizes into a tetragonal unit cell within the same space group of CsMAFA.^[36–38] In this structure, the Cs⁺ cations locate in between two sheets of [Pb₂Br₅][−] leading to a layered structure along the *c* axis of the unit cell. This phase has been employed in advanced green-emitting devices and laser applications owing to its sharp emission at around 550 nm, with a PLQY reported between 35% and 87%.^[38–41] This non-equilibrium phase segregation induced by moisture is highly anisotropic, as testified by the strong preferential orientation along the (001) planes. There is no consensual report about its bandgap value in literature. Indeed, although the previous studies agree upon the fact that CsPb₂Br₅ seems to have an indirect bandgap with a relatively low absorption coefficient compared to the perovskite CsMAFA, some of these studies reported a bandgap value greater than 3.1 eV on single crystals and as-synthesized powder.^[34] and a bandgap of ca. 2.4 eV on capped quantum dots or nanocrystals.^[38] In our case, we synthesized small single crystals of CsPb₂Br₅ according to the procedure reported in the experimental section^[42] and found that CsPb₂Br₅ has two very clear transitions at 2.32 eV and a more predominant in the UV at 3.42 eV (Figure S2). In a previous report by Hu et al.,^[43] phase segregation involving cesium was highlighted upon CsMAFA exposure under humidity (75% RH). The authors attributed the cesium segregated phase to a mixed halides CsPb₂I₄Br based on elemental quantification carried out by energy-dispersive X-ray spectroscopy (EDX). While the mixed halides CsPb₂Br_{5-x}I_x solid solution as proposed by Hu et al. appears thermodynamically not favorable, the attempts to synthesize this type of composition with different *x* values systematically led to a two-phase product, CsPb₂Br₅ on the one hand and CsPb₂I₅ on the other hand (Figure S3). These two phases, which are ion exchange materials, are isostructural with lattice cell parameters relatively close to each other.

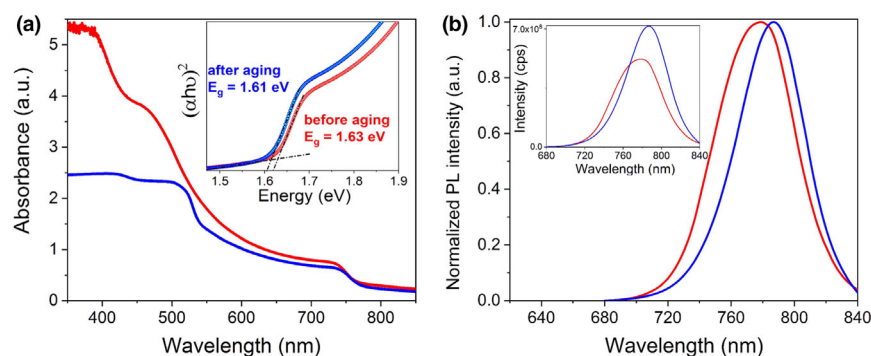


Figure 1. Comparison of fresh (red) and aged (1000 min under 85% RH, blue) CsMAFA thin film characterized by a) UV-Visible absorption spectroscopy along with the related Tauc plot assuming a direct allowed transition (in inset), b) normalized steady-state PL measured at 450 nm excitation wavelength. In inset, the same spectra are reported without normalization of the PL intensity.

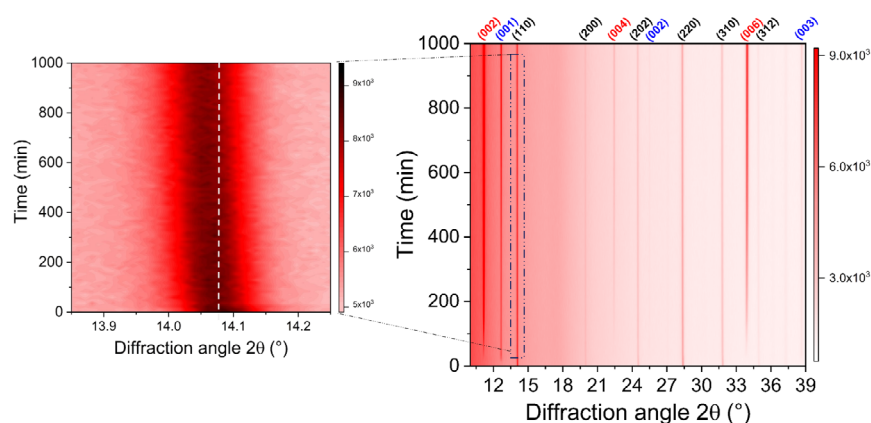


Figure 2. In situ X-ray diffraction patterns in contour plot of CsMAFA film as a function of aging time until 1000 min under 85% RH. The color of the different crystallographic orientations in black, blue, and red is corresponding to the CsMAFA perovskite, PbI_2 , and the segregated phase CsPb_2Br_5 . The left zoom-in contour plot shows the evolution of the main (110) diffraction peak of CsMAFA upon aging.

Owing to the decomposition into PbI_2 and the phase segregation into the pure inorganic lead bromide CsPb_2Br_5 , the remaining CsMAFA perovskite has a final stoichiometry modified compared to the pristine $\text{Cs}_{0.05}(\text{MA}_{0.17}\text{FA}_{0.83})_{0.95}\text{Pb}(\text{Br}_{0.17}\text{I}_{0.83})_3$. A closer inspection of the most intense diffraction peak of the (110) plane of CsMAFA between $2\theta = 13.9^\circ$ and 14.2° reveals a notable shift to lower angles upon aging, thus confirming the stoichiometry modification (Figure 2). All diffraction patterns have been refined in full-pattern matching mode to determine the evolution of lattice cell parameters before (Figure 3a) and during aging (Figure S4). As expected from the continuous shift to lower angles, both a and c parameters swelling are following a logarithmic-type trend. It leads to a volume cell expansion of ca. 0.5% from $994.4(2) \text{ \AA}^3$ to $999.4(1) \text{ \AA}^3$, for which the perovskite structure can easily accommodate without going through a phase transition. Based on these results, we reasoned that the aged CsMAFA is cesium and bromide poorer and iodide richer, which is consistent with the slight bandgap narrowing, the PL red-shift and possibly explain the higher PL intensity as previously pointed out by Herz et al.^[44] who showed higher PL yield for iodide-rich compositions. Cesium cation size is 167 pm, significantly

smaller than methylammonium (217 pm) and formamidinium (253 pm) counterparts, and iodide is 220 pm larger than bromide (196 pm), thus corroborating the lattice cell swelling.^[45,46] In the case of CsMAFA degradation, there is no evidence of the formation of a hydrated phase, which is contrast to the degradation of MAPbI_3 .^[30] All diffraction peaks collected at the end of the aging experiment can be totally refined with three phases, namely, CsMAFA, PbI_2 , and CsPb_2Br_5 (Figure 3b). The lattice cell parameters refined for CsPb_2Br_5 are $a = 8.356 \text{ \AA}$ and $c = 15.840 \text{ \AA}$, in agreement with the values reported in the literature.^[47]

To follow the dynamics of both CsMAFA decomposition into PbI_2 and phase segregation, Figure 3c reports the intensity evolution as a function of aging time of the most intense diffraction peak of CsMAFA, PbI_2 , and CsPb_2Br_5 .

The decomposition of CsMAFA into PbI_2 occurs in two stages. During an early stage of degradation (first hour), a rapid decomposition of CsMAFA into PbI_2 is observed, which then monotonously increases but at a slower rate until the end of the experiment. CsMAFA non-equilibrium segregation also starts once the film is exposed to moisture. The evolution kinetics is totally different, suggesting that decomposition and phase segregation are decoupled (degradation paths). Indeed, the segregation of CsMAFA is continuous and linear all along the aging experiment. Assuming this linear relationship, one can estimate by extrapolation (of 110 peak of CsMAFA until zero) that this latter will be completely segregated after ca. 650 h aging, a number well below the standard IEC61215 and IEC61646 aging test protocols.

Similar in situ XRD experiments were repeated for a CsMAFA layer infiltrated into a mesoporous scaffold of TiO_2 or underneath spiro-OMeTAD hole transporting layer (Figure S5). The degradation products are rigorously the same—excluding the contact layers—with the same strong preferential orientation for the growth of PbI_2 and for the phase segregated CsPb_2Br_5 . Therefore, the interfaces of the CsMAFA with the ETL and HTL are not influencing these thermodynamic aspects. The kinetics of these two processes is slightly modified owing to a change in accessibility for the water molecules to react with the perovskite and change in hydrophilicity of the surface when sheltered with the HTL. Indeed, some water molecules can remain adsorbed on the surface of TiO_2 nanocrystals or react with the dopants introduced into the spiro-OMeTAD, which are hygroscopic (Figure S5).^[48] Quantification of the different phases, in this case, is rather difficult to obtain by X-ray diffraction because of the strong preferential orientations of the phase formed. However, considering the decrease in intensity of the (110) plane of CsMAFA, we evaluate that both TiO_2 and spiro-OMeTAD reduce slightly the total amount of CsMAFA degraded.

Top-view low- and high-magnification representative scanning electron microscopy (SEM) images of fresh and aged CsMAFA reveal significant changes in the film morphology (Figure S6). The film

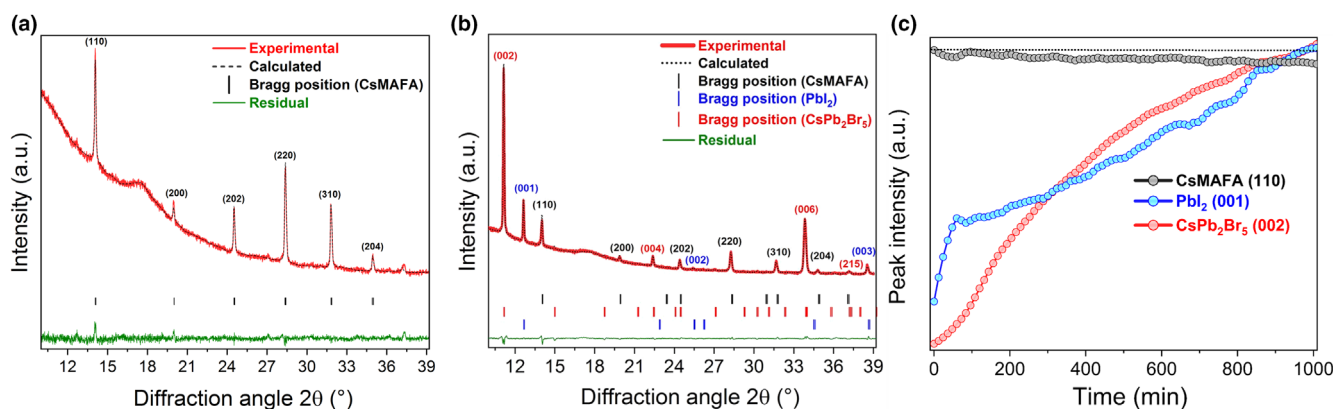


Figure 3. Full-pattern matching refinement of the X-ray diffractogram of CsMAFA film a) before and b) after aging including three different phases, CsMAFA in black, PbI_2 in blue, and CsPb_2Br_5 in red. c) Evolution of the X-ray diffraction peak intensity as a function of aging time for the (110) plane of CsMAFA (black), (001) plane of PbI_2 (blue), and (002) plane of CsPb_2Br_5 (red).

before aging is smooth, pinholes and crack-free. The smaller grains are corresponding to the PbI_2 nanoparticles resulting from its slight excess into the precursor solution (9 mol. %). However, after 1000-min exposure, the film becomes rougher and contains multiple pinholes, and long cracks are observed, testifying to the importance of the internal stress exerted by the aging process. The aged film is also composed of hierarchical tree-like regions of ca. 100 μm size, acicular particles, and well-shaped hexagonal particles of ca. 1 μm size. Emission lifetime for perovskite film is known to be sensitive to the film's morphology and topology. Therefore, the distribution of emission intensity and lifetime on CsMAFA films before and after aging were investigated using a fluorescence lifetime imaging microscope (FLIM). A square surface of 100 \times 100 μm (128 \times 128 pixels, 4 ms per pixels) was scanned, and its average lifetime in intensity is shown in **Figure 4** and **Figure S7**. As the experiments on films with segregated regions are sample and position-dependent, two different samples, two different areas, and four different depths of analysis were investigated to assess the PL behavior more precisely in the entire film. To avoid photo-degradation and to be in an excitation regime comparable with A.M. 1.5 G conditions, low power excitation was used. The overall emission decay for all pixels was fitted using two or three exponentials with a time constant ranging from few tens of nanoseconds to hundreds of nanoseconds (**Table S1**). Before aging, emission and average lifetimes are homogenous (**Figure 4a,b**, **Figure S7a**), and the existence of morphological defects is leading to a slight decrease in the average lifetime. The main time constants (contribution in amplitude) are the hundreds of nanoseconds (**Table S1**). After aging, the films are clearly more heterogeneous with a lower average lifetime (**Figure 4c,d**, **Figure S7b**). Looking more carefully at the emission lifetime, aging leads to the promotion of a fast component in few tens of nanoseconds, becoming the main component of the emission decay (**Table S1**, **Figure 4f**). Concomitantly to the existence of this short component, using an iCCD camera emission spectra is showing that aged film is characterized by an extra of at least two broad emission bands located between 550 and 700 nm attributed to the emission of PbI_2 , CsPb_2Br_5 , and possible contribution from the degraded CsMAFA remaining in the film (**Figure 4e**). No models are actually existing to account for such complex time-resolved PL decays. Its complexity stems from the multiple interfaces created after aging and possible

mixed contributions from bulk and surface of the perovskite grains in accordance with the more intricate steady-state PL.

In complement with the morphological and structural features at different scales and the long-range order measured by in situ X-ray diffraction, the results are corroborated with solid-state NMR spectroscopy to elucidate the local structures and interactions. We examined the ^1H and ^{133}Cs nuclei in fresh and aged CsMAFA materials to probe the changes in the short-range environment of cations upon exposure to moisture. Indeed, the sub-nanometer sensitivity and resolution associated with solid-state NMR spectroscopy allow the local chemical environments of organic and inorganic moieties, organic-organic, and organic-inorganic interfaces in photovoltaic materials to be characterized and distinguished.^[49–53] In particular, 1D and 2D (ss)NMR techniques have been employed to characterize local structures and site-specific dynamics in hybrid halide perovskites.^[12,30,51,52,54–58] The intrinsically high natural abundance (100%) associated with ^1H and ^{133}Cs MAS NMR^[57,59] allows the identification of different cation environments in CsMAFA. For the fresh material, a broad ^{133}Cs signal centered at ~ 31 ppm is attributed to the Cs^+ cation in the CsMAFA framework (**Figure 5a**). In the case of the aged CsMAFA, an additional broad distribution of the signal is observed in the range 220–300 ppm, which could be attributed to the Cs^+ ions located outside the CsMAFA framework as expected from the phase segregation revealed by X-ray diffraction analyses. Interestingly, the aged CsMAFA still contains some cesium cations in the 3D structure in light of the remaining ^{133}Cs signal at ~ 31 ppm. To corroborate the attribution of the broad signal intensity (200–300 ppm) measured for the aged CsMAFA film to different degradation products, 1D ^{133}Cs MAS NMR spectra of the synthesized powders of different stoichiometric combinations such as $1\text{CsI}:2\text{PbBr}_2$ and $1\text{CsI}:2\text{PbI}_2$ were acquired and compared. Previous literature suggests that the ^{133}Cs signal of CsI resonates in ~ 270 ppm. Therefore, it cannot be ruled out that the CsI as a plausible by-product. The signals observed in the range of 220–250 ppm correspond to the different local chemical environments of Cs^+ ions in these two inorganic materials. While these results do not directly rule out the possibility of CsPb_2I_5 forming, the X-ray and electron diffraction studies have not confirmed the occurrence of this phase. It thus highlights other possible types of Cs^+ ions in the aged film, such as more complex Cs-based polycrystalline degradation product(s), which are difficult to deconvolute and identify due to minuscule concentrations of locally

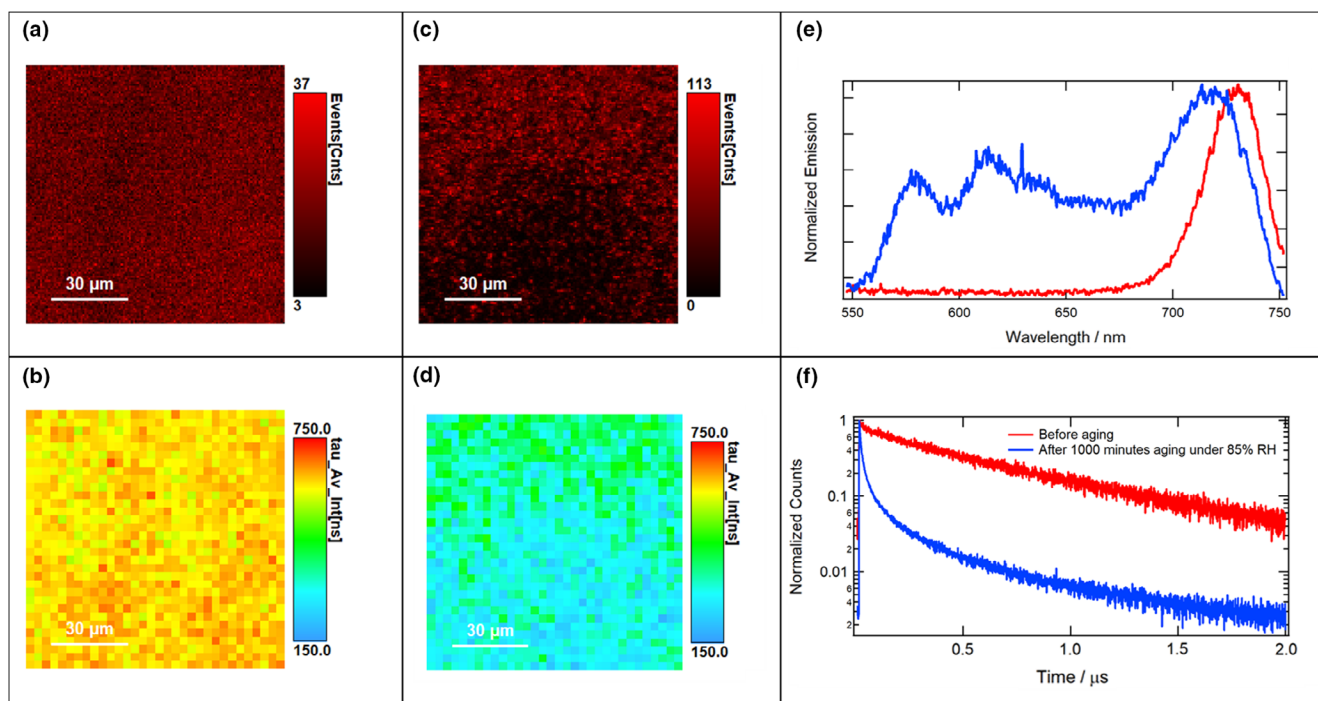


Figure 4. Microscopic emission imaging (a, c: Intensity; b, d: Average Lifetime) of CsMAFA thin film a, b) before and c, d) after 1000 min aging under 85% RH. Comparison of e) emission spectra (not corrected) and f) emission decay. A diode laser at 470 nm (500 kHz, 100 ps FWHM) was used, and emission was collected after a 498-nm long-pass filter. Note the difference of intensity scale between panels a and c.

ordered and disordered phases. This hypothesis is in line with X-ray diffraction results, as in the case of the aged film, a broad contribution at around $2\theta \approx 18^\circ$ is observed, suggesting the formation of poor crystalline phases in the film. In addition, residual quadrupolar broadening and local disorder associated with Cs^+ ions in degraded products may also contribute to the signal broadening (220–300 ppm), as is also observed for Cs^+ ions located in the perovskite framework (10–70 ppm).

Next, the local environments and through-space proximities between MA^+ and FA^+ cations in fresh and aged CsMAFA films were characterized by 1D and 2D ^1H NMR spectroscopy. Figure 5b,c (projection) compares the 1D ^1H MAS NMR spectra of as-synthesized and moisture exposed CsMAFA. In the case of fresh CsMAFA, ^1H signals at 3.4 and 6.3 ppm correspond to the methyl and ammonium protons of MA^+ , and the signals at 7.4 and 8.2 ppm correspond to the ammonium and methylene protons of FA^+ , respectively. The same material upon exposure to moisture (85% RH, 1000 min) exhibited identical ^1H signals, indicating that the organic cations are located in the perovskite framework in contrast to the Cs^+ ions. There is no ^1H signal corresponding to the degraded by-products of MA^+ or FA^+ , thus further confirming that the segregated Cs-based phases are purely inorganic without co-inclusion of organic units into its structure. In addition, the signal narrowing is observed in the ^1H spectrum of aged CsMAFA, which could be attributable to the well-ordered MA^+ and FA^+ cations. These results are further corroborated by the 2D ^1H - ^1H spin-diffusion NMR measurements and analyses of 1000 min aged CsMAFA (85% RH) material (Figure 5c). In a spin-diffusion experiment, magnetization is allowed to exchange between spatially proximate and dipolar coupled spins as a function of spin-diffusion time (also referred to as

mixing time). The resulting 2D spectrum contains on- and off-diagonal peaks, whereby off-diagonal peaks are characteristic of the magnetization exchange between inter- and intramolecular ^1H sites. In the case of aged CsMAFA, the off-diagonal 2D correlation peaks at $3.4 \leftrightarrow 6.3$ ppm shown in the blue shaded region indicate the magnetization exchange between intramolecular ^1H - ^1H proximities between CH_3 and NH_3 groups in MA^+ cations, and the off-diagonal peaks at $7.4 \leftrightarrow 8.2$ ppm shown in the green shaded region are attributed to magnetization exchange between CH and $(\text{NH}_2)_2$ groups in FA^+ cations of CsMAFA. The most notable is the 2D correlation peaks highlighted in the orange shaded region at $(3.4 \leftrightarrow 7.4$ ppm and $3.4 \leftrightarrow 8.2$ ppm, and $6.3 \leftrightarrow 7.4$ ppm and $6.3 \leftrightarrow 8.2$ ppm) which indicate the intermolecular $\text{MA}^+ \cdots \text{FA}^+$ proximities. These results and analyses reveal that the MA^+ and FA^+ cations are intermixed at the sub-nano- to nanometer length scale, retaining the 3D nature of CsMAFA even after 1000 min of exposure to 85% RH.

We achieved live observation of CsMAFA degradation in contact with water by in situ liquid-cell TEM experiments. In situ TEM is an effective advanced and challenging technique to visualize microstructural aspects and changes in the materials in real-time conditions. Recently, several direct observation studies using in situ TEM have highlighted fascinating results when analyzing the perovskite's thermal degradation.^[60–62] In situ liquid-cell electron microscopy allowed the dynamic observation of nanomaterial's crystallization processes in solution.^[63–66] However, this method has never been considered in PSCs since very recently by our group. We reported for the first time live observations of the moisture-induced degradation of MAPbI_3 in contact with water molecules showing morphological change and interfacial dissolution/recrystallization process accounting for the

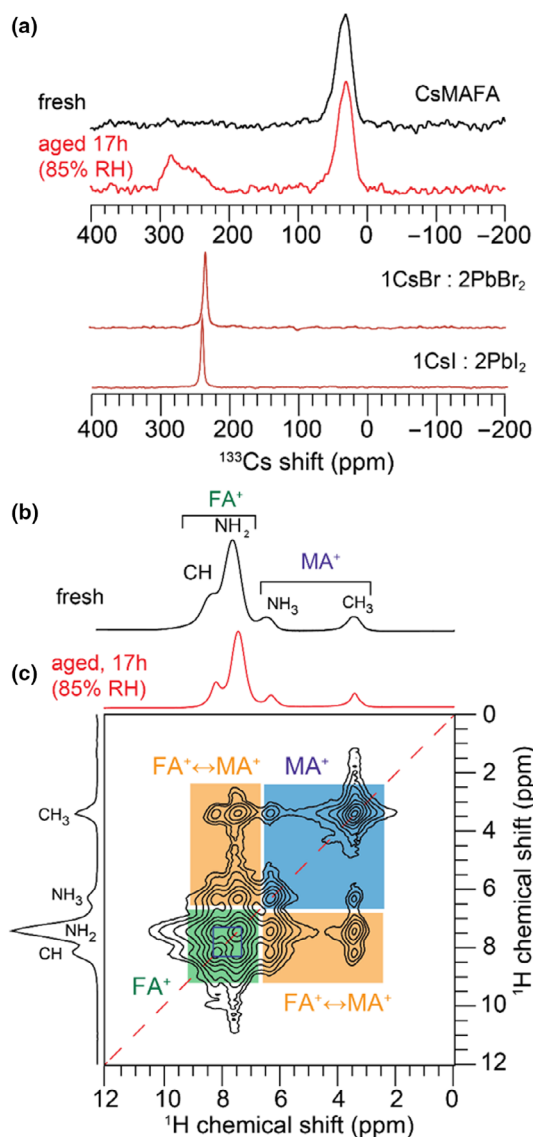


Figure 5. a) Solid-state 1D ^{133}Cs MAS NMR spectra of fresh and aged CsMAFA for 1000 min of moisture exposure at 85% RH, together with the 1D ^{133}Cs MAS NMR spectra of synthesized powers of $1\text{CsBr}:2\text{PbBr}_2$ and $1\text{CsI}:2\text{PbI}_2$. b) Solid-state 1D ^1H MAS spectra of fresh CsMAFA, and c) solid-state 2D ^1H - ^1H spin-diffusion spectrum of aged CsMAFA acquired using $t_{\text{mix}} = 500$ ms plotted with 1D ^1H skyline projections in the horizontal and vertical dimensions. ^1H signals corresponding to distinct proton sites are indicated. All spectra of CsMAFA were acquired at 18.8 T (^1H , 800.1 MHz, and ^{133}Cs , 104.9 MHz) with 50 kHz MAS, and the spectra of CsPb_2Br_5 and CsPb_2I_5 were acquired with 20 kHz MAS.

formation mechanism of PbI_2 crystals.^[30] For the experiment presented in this study, the CsMAFA perovskite layer was deposited on the top of the E-chip (Protochips) equipped with electron transparent amorphous silicon nitride (Si_3N_4) windows (experimental section). A scheme of the liquid cell utilized in this study is presented in Figure S8a. The chip was first characterized by SEM (Figure S8b). The images show a uniform coverage of the substrate, including well-packed grains of ca. 500 nm size with no visible pinholes and cracks over the amorphous silicon nitride window. In situ liquid-cell TEM

experiments provide a clear and live assessment about the degradation of CsMAFA exposed to water molecules, involving the formation and growth of different morphologies at the nanoscale (live movie shown in Supporting Information). Figure 6 and Movie S1 show firstly the perovskite dissolution, which is initiated by water contact and then followed by growth evolution. Depth analysis of the images collected raises two key observations. First, it shows the growth of large hexagonal-shaped particles in different parts of the film locations corresponding to the first 60 s of water contact (Figure 6b, Movie S1). Second, we can observe the growth of secondary needle-like (and hexagonal-like morphologies), growing preferentially in one direction (Figure 6c, Movie S1). The evolution of the transparent area of the image, which corresponds to electrons passing through the fluid and the silicon nitride window, was analyzed (Figure 6d). It shows at first less scattered points growth (blue curve) and a second one (red curve) containing a more scattered dataset owing to the non-simultaneous expansion of several particles along with the 2D projection of the image.

Figure S9 shows the STEM images corresponding to (specific) areas depicting particles of different morphologies with the corresponding selected area electron diffraction (SAED). The length of the needle-shaped particles is identified as PbI_2 and can reach up to 5 μm (Figure S9d). This phase can be ascribed to two types of above-observed morphologies, that is, the regular hexagonal particles and the sharp needles. PbI_2 growth is known to be governed by different external conditions; therefore, it is not surprising to find different morphologies for PbI_2 particles. The morphology of PbI_2 is tightly related to local variations, for example, pH, concentration, and other factors, leading to different morphologies.^[67,68] More prolonged exposure to moisture leads the crystals to lose their geometrical shape and split into several crystalline particles, as shown in Figure S10. Finally, the electron diffraction study also confirms the presence of segregated CsPb_2Br_5 among the hexagonal particles, as shown in inset in Figure S9e.

3. Conclusions

Combining advanced in situ characterization techniques with solid-state NMR, this work elucidates the degradation pathways of CsMAFA under moisture, which is crucial for understanding the environmental stability of perovskite-based photovoltaics. Based on these techniques, we demonstrate two concomitant degradation mechanisms, that is, the decomposition of CsMAFA into PbI_2 through a dissolution/recrystallization mechanism leading to needles and hexagonal shape particles and solid-state phase segregation leading to a Cs poorer and iodide richer CsMAFA phase on one side and CsPb_2Br_5 nanocrystals on other side. We reveal that this degradation mechanism is influenced neither by the contact with TiO_2 nor by the Spiro-OMeTAD, which are giving very similar results with only slight modification on kinetics. This is in stark contrast with MAPbI_3 , for which ETL and HTL contacts were modifying the moisture-induced degradation of the absorber substantially. Indeed, in the case of the latter, we evidenced a key relationship between degradation and the level of surface defects, which is not the case in CsMAFA. As a consequence, this work suggests that the degradation of CsMAFA under humidity is intrinsic-driven and is favored by the disordering created by mixing different monovalent cations and anions of very different sizes and properties in the perovskite structure rather than governed by surface point defects as for MAPbI_3 . Stabilizing in long-term such intricate compositions is thus expected to be highly

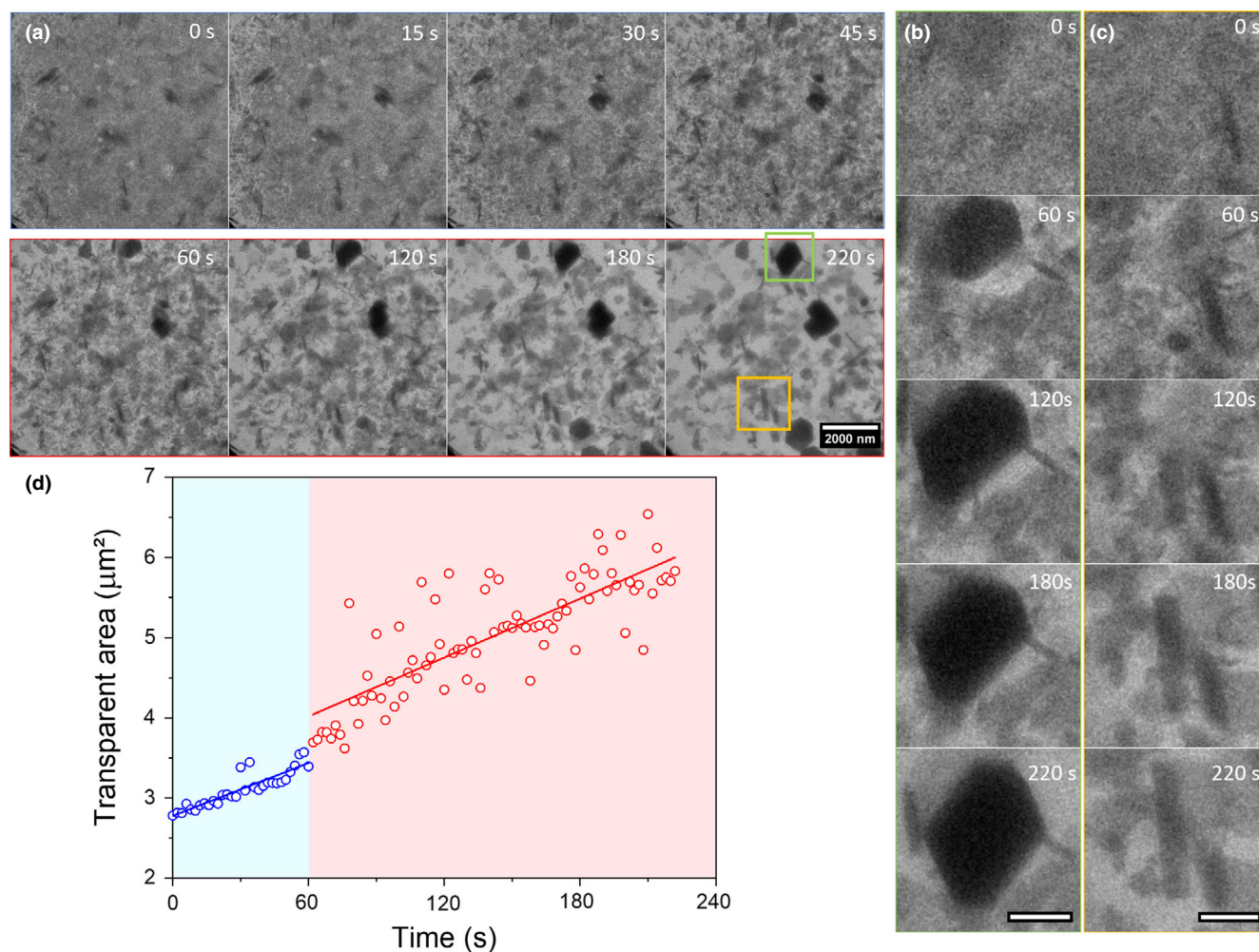


Figure 6. a) TEM imaging of CsMAFA changing in water between 0 and 220 s (scale bars are 1 μm). Growth of b) hexagonal-shaped and c) needle hexagonal-like particles in H_2O tracked by TEM as a function of time (scale bars are 500 nm). d) Growth of the transparent area of the image as a function of time between 0–60 s (blue) and 60–220 s (red).

complex given the high metastability character in contact with water molecules, and possibly same for other external stresses. A chance to succeed is either the tailoring of an additional hydrophobic layer in the device stack, the introduction of an external robust encapsulation barrier, or a step back to simpler compositions.

4. Experimental Section

Materials synthesis and processing: Unless specified, all chemicals were purchased from Sigma-Aldrich. Mesoporous TiO_2 paste and FK209 were purchased from GreatCell Solar. PbI_2 , PbBr_2 and CsI were purchased from TCI. CsBr was purchased from Alfa Aesar. FAI and MABr were purchased from Dyenamo. Glass substrate was used for in situ XRD experiments to avoid additional diffraction peaks from the transparent conducting oxide layer. Glass substrate or FTO glass substrate (TEC11L) was systematically cleaned with 2 vol.% of hellmanex solution in DI water, isopropanol and acetone (Sigma-Aldrich), and treated with UV- O_3 cleaner for 15 min prior usage. The CsMAFA precursor solution was prepared by dissolving 1.1 mol L^{-1} PbI_2 (508 mg), 0.22 mol L^{-1} PbBr_2 (80.7 mg), 1 mol L^{-1} FAI (172 mg), 0.20 mol L^{-1} MABr (22.4 mg), and 0.06 mol L^{-1} CsI (17.5 mg) in anhydrous N,N -dimethylformamide (Sigma-Aldrich) and anhydrous dimethyl sulfoxide (Sigma-Aldrich) with 4:1 ratio (v/v), respectively. The solution was kept at

70 $^\circ\text{C}$ for 2 h under stirring and then cooled down to ambient temperature and filtrated through a 0.45- μm syringe filter, yielding a nominal composition of $\text{Cs}_{0.05}(\text{FA}_{0.83}\text{MA}_{0.17})_{0.95}\text{Pb}(\text{I}_{0.83}\text{Br}_{0.17})_3$. The solution was spin-coated according to a two-step procedure inside an Ar-filled glovebox (MBraun Unilab Pro SP), first at 2000 rpm for 10 s and then 4000 rpm for 20 s. During the second step, 100 μL of chlorobenzene as an anti-solvent was dropped 10 s before the program's end. These films were annealed at 110 $^\circ\text{C}$ for 45 min inside the glovebox to crystallize the perovskite structure leading to a mirror-like dark film. This procedure has been optimized to reach the highest power conversion efficiency in full devices, and ca. 20% PCE is obtained typically on average. It leads to films with the same thickness (350 ± 10 nm).

The CsPb_2Br_5 powder was synthesized by crystallization reaction of lead bromide (1.4 mmol) and cesium bromide (0.7 mmol). They were dissolved in 6 mL of HBr (HBr, 48%, Fisher chemicals). The mixture was heated at 118 $^\circ\text{C}$ and stirred overnight. After that, the reaction vessel was led to cool down at room temperature, and the precipitates were collected by vacuum filtration and washed by diethyl ether. The precipitates were dried under vacuum at 60 $^\circ\text{C}$ to obtain the powder. Different cesium lead Br/I stoichiometry powders were prepared by crystallization method (detailed for the synthesis of CsPb_2Br_5) of various precursor salts (PbI_2 : PbBr_2 : CsBr : CsI) in HBr. The total concentration of these precursor salts was similar to the concentration used in the synthesis of CsPb_2Br_5 . CsPb_2I_5 was synthesized by a halogen exchange reaction from CsPb_2Br_5 . This reaction was performed under argon flow controlled through the Schlenk line system. The

equimolar amount of CsPb₂Br₅ powders and lead iodide (PbI₂) was mixed in 21 mL of 1-octadecene (20 mL, 90%, Alfa Aesar), oleic acid (0.5 mL, 90%, Alfa Aesar), and oleylamine (0.5 mL, 70%, Sigma-Aldrich). The reaction was heated at 160 °C for overnight. After cooling down to room temperature, the product was collected by vacuum filtration and washed with ethyl ether. It was then dried at 60 °C for 4 h in vacuum and sintered at 160 °C for 30 min.

The X-ray diffraction study was carried out at room temperature on a Bruker D8 diffractometer using a copper anti-cathode ($\lambda_{\text{CuK}\alpha 1} = 1.54056 \text{ \AA}$ and $\lambda_{\text{CuK}\alpha 2} = 1.54439 \text{ \AA}$) equipped with a LynxEye detector. Each pattern was collected within 11 min from $2\theta = 10^\circ$ to 40° with a step size of 0.01° . For in situ measurements under a controlled humid atmosphere, an Anton Paar HTK furnace has been modified to allow very precise humidity production and control all over the experiment. The RH level was monitored at both the inlet and outlet of the sample chamber to ensure moisture-level homogeneity to $85 \pm 5\%$ RH.

In situ TEM experiments were performed using a FEI Tecnai F20 microscope equipped with a cold FEG. The sample of CsMAFA was deposited by spin coating onto an E-chip (Protochips) equipped with electron transparent amorphous silicon nitride (Si₃N₄) windows with a thickness of 30 nm. For spin coating, 0.5 mol L⁻¹ precursor solution was used within an Ar-filled glovebox, first at 3000 rpm for 10 s and 6000 rpm for 20 s. During the second step, 100 μL of chlorobenzene as an anti-solvent was dropped 10 s before the end of the program. The E-chip was post-annealed at 110 °C for 30 min inside the glovebox leading to a film thickness of ca. 200 nm. Under a binocular, the liquid cell is mounted in the TEM holder in a sandwich configuration with a sample top chip and a spacer bottom chip. Both chips are in contact with a two-level O-ring gasket to ensure good sealing. The spacer chip fixes a gap of 1 μm for the liquid flow. The lid of the TEM sample holder is screwed on top with a clamping force fixed by a torque screwdriver. The sealing is then tested before the insertion in the TEM with a turbo pump (10^{-9} Torr). While the sample holder is inserted and kept under vacuum in the pumping station, the pressure value should remain steady. Then, the plugs of the internal fluidic tubing circuit (inlets and outlets) are unscrewed one after the other to check that there is no pressure variation. After 20 min of this sealing test, all plugs are put back. The specimen holder is then inserted in the TEM, and the plugs of inlet and outlet are removed. The inlet is connected via a PEEK tubing set to a 5-mL syringe filled with water mounted on a pump, and the outlet is connected to a vial equipped with a septum so that the whole circuit is sealed prior to the liquid injection, and the pristine CsMAFA layer was characterized by TEM, STEM-HAADF imaging, and SAED. Water was injected inside the liquid cell using a syringe pump with a flow rate of 5 $\mu\text{L min}^{-1}$, which has been maintained during the in situ experiment. The thickness of liquid in the cell depends on the spacer that fixes a gap of 1 μm between the chip. The evolution of the sample upon the time of exposure was followed by TEM imaging with a Gatan Oneview CMOS camera. The high spatial resolution and the sensibility of this camera allowed video sequences to be recorded in 4K with an exposition of 20–40 ms per image, corresponding to rates of 25–50 images per second. This sensibility also allows to collect SAED with a good intensity resolution in 4K images with 32 bits for gray levels. All measurements were performed with 200 kV acceleration voltage. TEM images are collected using low electron dose rate, from 0.1 to 2.4 $\text{e} \text{ \AA}^{-2} \text{ s}^{-1}$. The dose is extracted through GMS3 DigitalMicrograph[®] software. The growth study of single particles while CsMAFA degradation in water was analyzed using the WEKA random-forest segmentation 3D plugin of the software ImageJ. The SAED patterns were acquired operating with a precession angle of 0.7 degrees and precession frequency of 100 Hz. The identification of diffraction patterns was proceeded using ASTAR Nanomegas and MacTempaX software.

For solid-state NMR spectroscopy experiments, Cs_{0.05}(MA_{0.17}FA_{0.83})_{0.95}Pb(Br_{0.17}I_{0.83})₃ (CsMAFA) films spin-coated on glass substrates were scratched to obtain approximately 12 mg of the powder. Scratched CsMAFA powder was exposed to moisture ($85 \pm 5\%$ RH) for 1000 min in a humidity-controlled hydration chamber. The humidity level was monitored using a hygrometer placed inside the hydration chamber. The sample was packed into a 1.3 mm rotor closed with Vespel[®] caps. All 1D ¹H and ¹³³Cs NMR experiments of fresh and aged CsMAFA materials were carried out on a Bruker Avance Neo (18.8 T, ¹H Larmor frequency = 800.1 MHz) spectrometer using a double-resonance H-X 1.3 mm MAS probe. The MAS frequency was 50 kHz. The nutation frequency of ¹H was 192.3 kHz, corresponding to a 90° pulse duration of 1.3 μs . The ¹H spin-lattice relaxation times (T_1) were determined to be 24 s for CH₃ and NH₃ protons

in methylammonium cation and 26 s for formamidinium cation in CsMAFA using inversion recovery measurements and analyses. 1D ¹H MAS NMR spectrum was acquired using 16 co-added transients and a recovery delay $\tau_{\text{RD}} = 32 \text{ s}$. 2D ¹H–¹H spin-diffusion (SD) NMR spectrum of aged CsMAFA (1000 min, 85% RH) was acquired with rotor synchronized 256 t_1 increments, corresponding to the total experimental time $T_{\text{exp}} = 2.3 \text{ h}$. The nutation frequency of ¹³³Cs was 69 kHz, which corresponds to a 90° pulse duration of 3.6 μs . 1D ¹³³Cs MAS NMR spectrum of fresh CsMAFA material was acquired using 192 co-added transients, corresponding to $T_{\text{exp}} = 5.1 \text{ h}$, and a ¹³³Cs MAS NMR spectra of the same material after exposure to moisture (1000 min) were acquired with 600 co-added transients, corresponding to $T_{\text{exp}} = 8.2 \text{ h}$. To understand the different distributions of ¹³³Cs signals in the aged CsMAFA material and identify different by-products, we separately carried out solid-state ¹³³Cs NMR experiments of CsPb₂Br₅ and CsPb₂I₅ materials and compared them. These materials were packed into a 3.2-mm rotor, and ¹³³Cs spectra were acquired using a double-resonance H-X 3.2 mm MAS probe at MAS frequency of 20 kHz. ¹³³Cs nutation frequency was 125 kHz corresponding to a 90° pulse duration of 2.0 μs . 1D ¹³³Cs spectra were acquired using 32 co-added transients corresponding to $T_{\text{exp}} = 34 \text{ min}$. The ¹H chemical shifts were calibrated with respect to neat TMS using adamantane as an external reference (¹H resonance, 1.8 ppm). The ¹³³Cs shifts were calibrated with respect to 0.1 M CsCl solution.

Scanning electron microscopy experiments were performed using an environmental FEI Quanta 200 FEG microscope. UV-Vis absorption spectra were recorded in absorbance mode using an Agilent Cary5000 UV-Vis-NIR spectrometer. Steady-state fluorescence and TCSPC were carried out on Edinburgh Instrument FLS980 spectrometer equipped with a 450W Xe arc lamp for steady-state measurements with two excitation/emission monochromators (excitation/emission bandwidth of 3 nm). Fluorescence lifetime images were obtained using a homemade confocal microscope setup. The excitation (100 ps, 470 nm, 6 nW, circular polarization, dichroic mirror at 488 nm, air objective 40 \times), emission collection pathway (long pass emission filter at 496 nm, confocal pinhole 100 μm , APD) and an inverted microscope (IX81). Piezostage and single-photon count card were different to be able to image 100 \times 100 μm area and detect longer photon arrival time. The sample was mounted here on a three-dimensional translation stage (P-562.3CD, Digital controller E-725.3CD, Physik Instrument), which allows raster scanning pixel-by-pixel an entire area of 200 \times 200 \times 200 μm (1 nm resolution) and controlled by commercial software (Symphotime64, Picoquant). Photon arrival time for each pixel was obtained using a TimeHarp 260 Picodual (25-ps bin time resolution), and calculation of average lifetime for each pixel was done by Symphotime64. The emission spectra were measured by adding a 50:50 non-polarized beam splitter between the pinhole and the APD. 50% of the collected emission light was focused into the slit of a spectrometer (Isoplane-160, grating 300 G mm⁻¹ blazed at 750 nm, calibration with a Mercury lamp, bandpass 2 nm) coupled to an Intensified back-illuminated emCCD camera (PI-MAX4-1024, GenIII filmless, Princeton Instrument). Pixel dwell time was fixed to 4 ms, and for average lifetime imaging calculation, images (128 \times 128 pixels) were rebinned by 4 and bin time by 16 (400 ps) to get enough photon statistics. The average lifetime in intensity was calculated by tailfit using a sum of 2 or 3 exponential decays from 26 ns to 2 μs . The quality of the fit was judged on the residuals and reduced χ^2 (<1.1) for the overall decay. Emission spectra were registered by accumulating all photons during the acquisition of one image.

Acknowledgements

This work has received financial support from Région Hauts-de-France, FEDER, and Electricité de France (EDF) through PEROVSTAB program. We thank the electronic microscopy platform of UPJV for access to SEM and TEM microscopes. Dr. Anurag Krishna (LRCS and EPFL), Dr. Sebastien Gottis (LRCS), and Dr. Jean-Noel Chotard (LRCS) are acknowledged for fruitful discussions. M.A.A.K and F.S. gratefully acknowledge the financial support from the IR-RMN-THC FR-3050 CNRS France for conducting solid-state NMR measurements. P.R. and G.N.M.R. acknowledge the financial support from University of Lille and région Hauts-de-France. F.S. acknowledges "IMPRESSIVE" project which received funding from the European Union's Horizon 2020 Research and Innovation Program under grant agreement number 826013.

Conflict of Interest

The authors declare no conflict of interest.

Supporting Information

Supporting Information is available from the Wiley Online Library or from the author.

Keywords

liquid-cell transmission electron microscopy, moisture degradation, perovskite stability, phase segregation, solid-state NMR

Received: September 30, 2021

Revised: November 18, 2021

Published online: November 30, 2021

- [1] Best Research-Cell Efficiency Chart. Photovoltaic Research. NREL.
- [2] R. E. Brandt, V. Stevanović, D. S. Ginley, T. Buonassisi, *MRS Commun.* **2015**, 5, 265.
- [3] M. Saliba, T. Matsui, K. Domanski, J.-Y. Seo, A. Ummadisingu, S. M. Zakeeruddin, J.-P. Correa-Baena, W. R. Tress, A. Abate, A. Hagfeldt, M. Grätzel, *Science* **2016**, 354, 206.
- [4] M. Saliba, T. Buonassisi, M. Grätzel, A. Abate, W. Tress, A. Hagfeldt, *Science* **2017**, 358, 739.
- [5] A. Al-Ashouri, E. Köhnen, B. Li, A. Magomedov, H. Hempel, P. Caprioglio, J. A. Márquez, A. B. Morales Vilches, E. Kasparavicius, J. A. Smith, N. Phung, D. Menzel, M. Grischek, L. Kegelmann, D. Skroblin, C. Gollwitzer, T. Malinauskas, M. Jošt, G. Matic, B. Rech, R. Schlatmann, M. Topič, L. Korte, A. Abate, B. Stannowski, D. Neher, M. Stollerfoht, T. Unold, V. Getautis, S. Albrecht, *Science* **2020**, 370, 1300.
- [6] A. Uddin, M. B. Upama, H. Yi, L. Duan, *Coatings* **2019**, 9, 65.
- [7] F. Corsini, G. Griffini, *J. Phys. Energy* **2020**, 2, 031002.
- [8] I. Hwang, I. Jeong, J. Lee, M. J. Ko, K. Yong, *ACS Appl. Mater. Interfaces* **2015**, 7, 17330.
- [9] A. Krishna, S. Gottis, M. K. Nazeeruddin, F. Sauvage, *Adv. Funct. Mater.* **2019**, 29, 1.
- [10] E. Aydin, M. Bastiani, S. Wolf, *Adv. Mater.* **2019**, 31, 1900428.
- [11] F. Gao, Y. Zhao, X. Zhang, J. You, *Adv. Energy Mater.* **2019**, 10, 1902650.
- [12] A. Krishna, M. A. Akhavan Kazemi, M. Sliwa, G. N. M. Reddy, L. Delevoye, O. Lafon, A. Felten, M. T. Do, S. Gottis, F. Sauvage, *Adv. Funct. Mater.* **2020**, 30, 1909737.
- [13] S. Akin, N. Arora, S. M. Zakeeruddin, M. Grätzel, R. H. Friend, M. I. Dar, *Adv. Energy Mater.* **2020**, 10, 1903090.
- [14] A. M. Askar, G. M. Bernard, B. Wiltshire, K. Shankar, V. K. Michaelis, *J. Phys. Chem. C* **2017**, 121, 1013.
- [15] N. Aristidou, I. Sanchez-Molina, T. Chotchuangchutchaval, M. Brown, L. Martinez, T. Rath, S. A. Haque, *Angew. Chem.* **2015**, 127, 8326.
- [16] B. Conings, J. Drijkoningen, N. Gauquelin, A. Babayigit, J. D'Haen, L. D'Olieslaeger, A. Ethirajan, J. Verbeeck, J. Manca, E. Mosconi, F. De Angelis, H. G. Boyen, *Adv. Energy Mater.* **2015**, 5, 1500477.
- [17] M. A. Leguy, Y. Hu, M. Campoy-quiles, M. I. Alonso, O. J. Weber, P. Azarhoosh, M. Van Schilfgaarde, M. T. Weller, T. Bein, J. Nelson, P. Docampo, P. R. F. Barnes, *Chem. Mater.* **2015**, 27, 3397.
- [18] H. S. Kim, J. Y. Seo, N. G. Park, *ChemSuschem* **2016**, 9, 2528.
- [19] I. Deretzis, E. Smecca, G. Mannino, A. La Magna, T. Miyasaka, A. Alberti, *J. Phys. Chem. Lett.* **2018**, 9, 3000.
- [20] Z. Song, N. Shrestha, S. C. Wathhage, G. K. Liyanage, Z. S. Almutawah, R. H. Ahangharnejhad, A. B. Phillips, R. J. Ellingson, M. J. Heben, *J. Phys. Chem. Lett.* **2018**, 9, 6312.
- [21] X. Tang, M. Van Den Berg, E. Gu, A. Horneber, G. J. Matt, A. Osvet, A. J. Meixner, D. Zhang, C. J. Brabec, *Nano Lett.* **2018**, 18, 2172.
- [22] S. Mahesh, J. M. Ball, R. D. J. Oliver, D. P. McMeekin, P. K. Nayak, M. B. Johnston, H. J. Snaith, *Energy Environ. Sci.* **2020**, 13, 258.
- [23] C. C. Boyd, R. Cheacharoen, T. Leijtens, M. D. McGehee, *Chem. Rev.* **2019**, 119, 3418.
- [24] E. T. Hoke, D. J. Slotcavage, E. R. Dohner, A. R. Bowering, H. I. Karunadasa, M. D. McGehee, *Chem. Sci.* **2014**, 6, 613.
- [25] A. J. Knight, L. M. Herz, *Energy Environ. Sci.* **2020**, 13, 2024.
- [26] A. J. Knight, J. Borchert, R. D. J. Oliver, J. B. Patel, P. G. Radaelli, H. J. Snaith, M. B. Johnston, L. M. Herz, *ACS Energy Lett.* **2021**, 6, 799.
- [27] F. Ruf, P. Rietz, M. F. Ayguler, I. Kelz, P. Docampo, H. Kalt, M. Hetterich, *ACS Energy Lett.* **2018**, 3, 2995.
- [28] J. M. Howard, E. M. Tennyson, S. Barik, R. Szostak, E. Waks, M. F. Toney, A. F. Nogueira, B. R. A. Neves, M. S. Leite, *J. Phys. Chem. Lett.* **2018**, 9, 3463.
- [29] J. Hidalgo, C. A. R. Perini, A.-F. Castro-Mendez, D. Jones, H. Kobler, B. Lai, R. Li, S. Sun, A. Abate, J.-P. Correa-Baena, *ACS Energy Lett.* **2020**, 5, 3526.
- [30] M. A. Akhavan Kazemi, P. Raval, K. Cherednicheko, J. N. Chotard, A. Krishna, A. Demortiere, G. N. M. Reddy, F. Sauvage, *Small Methods* **2020**, 5, 2000834.
- [31] H. Tan, F. Che, M. Wei, Y. Zhao, M. I. Saidaminov, P. Todorovi, D. Broberg, G. Walters, F. Tan, T. Zhuang, B. Sun, Z. Liang, H. Yuan, E. Fron, J. Kim, Z. Yang, O. Voznyy, M. Asta, E. H. Sargent, *Nat. Commun.* **2018**, 9, 1.
- [32] M. Shirayama, H. Kadowaki, T. Miyadera, T. Sugita, M. Takakoshi, M. Kato, T. Fujiseki, D. Murata, S. Hara, T. N. Murakami, S. Fujimoto, M. Chikamatsu, H. Fujiwara, *Phys. Rev. Appl.* **2016**, 5, 014012.
- [33] G. Grancini, V. D'Innocenzo, E. R. Dohner, N. Martino, A. R. Srimath Kandada, E. Mosconi, F. De Angelis, H. I. Karunadasa, E. T. Hoke, A. Petrozza, *Chem. Sci.* **2015**, 6, 7305.
- [34] H.-H. Fang, S. Adjokatse, H. Wei, J. Yang, G. R. Blake, J. Huang, J. Even, M. A. Loi, *Sci. Adv.* **2016**, 2, e1600534.
- [35] G. E. Peron, S. N. Habisreutinger, T. Leijtens, B. J. Bruijns, J. J. van Franeker, D. W. DeQuilettes, S. J. Pathak, R. J. Sutton, G. Grancini, D. S. Ginger, R. A. J. Janssen, A. Petrozza, H. J. Snaith, *ACS Nano* **2015**, 9, 9380.
- [36] I. Dursun, M. De Bastiani, B. Tureli, B. Alamer, O. F. Mohammed, M. Eddaoudi, O. M. Bakr, *ChemSuschem* **2017**, 10, 3746.
- [37] G. Li, H. Wang, Z. Zhu, Y. Chang, T. Zhang, Z. Song, Y. Jiang, *Chem. Commun.* **2016**, 52, 11296.
- [38] X. Tang, Z. Hu, W. Yuan, W. Hu, H. Shao, D. Han, *Adv. Opt. Mater.* **2017**, 5, 1600788.
- [39] K. Wang, L. Wu, L. Li, H. Yao, H. Qian, S. Yu, *Angew. Chem. Int. Ed.* **2016**, 55, 8328.
- [40] X. Zhang, B. Xu, J. Zhang, Y. Gao, Y. Zheng, K. Wang, W. Sun, *Adv. Funct. Mater.* **2016**, 26, 4595.
- [41] C. Qin, T. Matsushima, A. S. D. Sandanayaka, Y. Tsuchiya, C. Adachi, *J. Phys. Chem. Lett.* **2017**, 8, 5415.
- [42] O. Nazarenko, M. R. Kotyba, M. Worle, E. Cuervo-Reyes, S. Yakunin, M. V. Kovalenko, *Inorg. Chem.* **2017**, 56, 11552.
- [43] Y. Hu, M. F. Ayguler, M. L. Petrus, T. Bein, P. Docampo, *ACS Energy Lett.* **2017**, 2, 2212.
- [44] W. Rehman, R. L. Milot, G. E. Peron, C. Wehrenfennig, J. L. Boland, H. J. Snaith, M. B. Johnston, L. M. Herz, *Adv. Mater.* **2015**, 27, 7938.
- [45] R. D. Shannon, *Acta Crystallogr. Sect. A* **1976**, 32, 751.
- [46] G. Kieslich, S. Sun, A. K. Cheetham, *Chem. Sci.* **2015**, 6, 3430.
- [47] J. Li, H. Zhang, S. Wang, D. Long, M. Li, Y. Guo, Z. Zhong, K. Wu, D. Wang, T. Zhang, *RSC Adv.* **2017**, 7, 54002.
- [48] T. A. Berhe, W. Su, C. Chen, C. Pan, J. Cheng, H. Chen, M. Tsai, L. Chen, A. A. Dubale, B. Hwang, *Energy Environ. Sci.* **2016**, 9, 323.
- [49] A. Karki, J. Vollbrecht, A. J. Gillett, S. S. Xiao, Y. Yang, Z. Peng, N. Schopp, S. Yoon, H. Ade, G. N. M. Reddy, R. H. Friend, T. Nguyen, *Energy Environ. Sci.* **2020**, 13, 3679.
- [50] A. Karki, J. Vollbrecht, A. L. Dixon, N. Schopp, M. Schrock, G. N. M. Reddy, T. Nguyen, *Adv. Mater.* **2019**, 31, 1903868.

- [51] M. Seifrid, G. N. M. Reddy, B. F. Chmelka, G. C. Bazan, *Nat. Rev. Mater.* **2020**, *5*, 910.
- [52] L. Piveteau, V. Morad, M. V. Kovalenko, *J. Am. Chem. Soc.* **2020**, *142*, 19413.
- [53] C. Tzschaschel, T. Satoh, M. Fiebig, *Nat. Commun.* **2019**, *10*, 1.
- [54] C. J. Dahlman, R. M. Kennard, P. Paluch, N. R. Venkatesan, M. L. Chabinyc, G. N. Manjunatha Reddy, *Chem. Mater.* **2021**, *33*, 642.
- [55] D. J. Kubicki, D. Prochowicz, E. Salager, A. Rakhmatullin, C. P. Grey, L. Emsley, S. D. Stranks, *J. Am. Chem. Soc.* **2020**, *142*, 7813.
- [56] D. J. Kubicki, D. Prochowicz, A. Hofstetter, P. Péchy, S. M. Zakeeruddin, M. Gratzel, L. Emsley, *J. Am. Chem. Soc.* **2017**, *139*, 10055.
- [57] A. Karmakar, M. S. Dodd, X. Zhang, M. S. Oakley, M. Klobukowski, V. K. Michaelis, *Chem. Commun.* **2019**, *55*, 5079.
- [58] C. J. Dahlman, D. J. Kubicki, G. N. M. Reddy, *J. Mater. Chem. A* **2021**, *9*, 19206.
- [59] A. Karmakar, A. Bhattacharya, D. Sarkar, G. M. Bernard, A. Mar, V. K. Michaelis, *Chem. Sci.* **2021**, *12*, 3253.
- [60] T. W. Kim, N. Shibayama, L. Cojocaru, S. Uchida, T. Kondo, H. Segawa, *Adv. Funct. Mater.* **2018**, *28*, 1804039.
- [61] F. U. Kosasih, C. Ducati, *Nano Energy* **2018**, *47*, 243.
- [62] Y. Zhou, H. Sternlicht, N. P. Padture, *Joule* **2019**, *3*, 641.
- [63] M. E. Holtz, Y. Yu, J. Gao, H. D. Abruña, D. A. Muller, *Microsc. Microanal.* **2013**, *19*, 1027.
- [64] H. Zheng, R. K. Smith, Y. Jun, C. Kisielowski, U. Dahmen, A. P. Alivisatos, *Science* **2009**, *324*, 1309.
- [65] T. J. Woehl, J. E. Evans, I. Arslan, W. D. Ristenpart, N. D. Browning, *ACS Nano* **2012**, *6*, 8599.
- [66] K. L. Jungjohann, S. Bliznakov, P. W. Sutter, E. A. Stach, E. A. Sutter, *Nano Lett.* **2013**, *13*, 2964.
- [67] Z. Zheng, A. Liu, S. Wang, Y. Wang, Z. Li, M. Lau, L. Zhang, *J. Mater. Chem.* **2005**, *15*, 4555.
- [68] G. Zhu, P. Liu, M. Hojamberdiev, J. Z. Xijin, H. Bo, F. Rong, *Appl. Phys. A* **2010**, *98*, 299.